Heliyon 8 (2022) e10831

Contents lists available at ScienceDirect

Heliyon

journal homepage: www.cell.com/heliyon

Research article

# Synthesis, spectroscopic, topological, hirshfeld surface analysis, and anti-covid-19 molecular docking investigation of isopropyl 1-benzoyl-4-(benzoyloxy)-2,6-diphenyl-1,2,5,6-tetrahydropyridine-3-carboxylate

Arulraj Ramalingam [a,**], Murugavel Kuppusamy [b,***], Sivakumar Sambandam [c], Mouna Medimagh [d], Oluwatoba Emmanuel Oyeneyin [e,*], Amirthaganesan Shanmugasundaram [f], Noureddine Issaoui [d], Nathanael Damilare Ojo [g]

[a] Department of Electrical and Computer Engineering, National University of Singapore, 117583, Singapore
[b] PG & Research Department of Chemistry, Government Arts College, Chidambaram, Tamil Nadu, India
[c] Research and Development Centre, Bharathiar University, Coimbatore 641 046, Tamil Nadu, India
[d] University of Monastir, Faculty of Sciences, Laboratory of Quantum and Statistical Physics (LR18ES18), Monastir, 5079, Tunisia
[e] Theoretical and Computational Chemistry Unit, Department of Chemical Sciences Adekunle Ajasin University, Akungba Akoko, Ondo State, Nigeria
[f] Department of Chemistry, Saveetha School of Engineering, Saveetha University, Chennai, Tamil Nadu, India
[g] Department of Chemistry, University of Ibadan, Oyo State, Nigeria

ARTICLE INFO

*Keywords:*
Tetrahydropyridine-3-carboxylate
Density functional theory
Severe acute respiratory syndrome-coronavirus disease
Hirshfeld surface analysis
Topological analysis

ABSTRACT

Isopropyl 1-benzoyl-4-(benzoyloxy)-2,6-diphenyl-1,2,5,6-tetrahydropyridine-3-carboxylate (IDPC) was synthesized and characterized via spectroscopic (FT-IR and NMR) techniques. Hirshfeld surface and topological analyses were conducted to study structural and molecular properties. The energy gap ($E_g$), frontier orbital energies ($E_{HOMO}$, $E_{LUMO}$) and reactivity parameters (like chemical hardness and global hardness) were calculated using density functional theory with B3LYP/6–311++G (d,p) level of theory. Molecular docking of IDPC at the active sites of SARS-COVID receptors was investigated. IDPC molecule crystallized in the centrosymmetric triclinic ($P\bar{1}$) space group. The topological and Hirshfeld surface analysis revealed that covalent, non-covalent and intermolecular H-bonding interactions, and electron delocalization exist in the molecular framework. Higher binding score (-6.966 kcal/mol) of IDPC at the active site of SARS-COVID main protease compared to other proteases suggests that IDPC has the potential of blocking polyprotein maturation. H-bonding and π-cationic and interactions of the phenyl ring and carbonyl oxygen of the ligand indicate the effective inhibiting potential of the compound against the virus.

## 1. Introduction

Heterocyclic compounds are planar rings of carbon atoms containing at least one heteroatom such as O, N, P and/or S in their structures [1, 2]. They are of interest to scientists and researchers because of their applications in different areas of materials and pharmaceutical research [3, 4, 5, 6]. Nitrogen heterocyclic compounds are important building blocks in the many bioactive natural products and commercial drugs. Piperidine-based heterocyclic amines are widely used as a building block in organic synthesis and drug discovery. Its compounds show a variety of biological activities viz; anticancer, antimicrobial, analgesic and anti-inflammatory agents. Piperidine and pyridine components are the most common heterocyclic fragments present in FDA approved drugs [7]. Instead of having a secondary amine group in the piperidine ring, the ring nitrogen substituted by alkyl, aryl, and carbonyl groups [8], acetyl or benzoyl group possesses more biological activity [9, 10]. Substituted

* Corresponding author.
** Corresponding author.
*** Corresponding author.
*E-mail addresses:* rarulraj108@gmail.com (A. Ramalingam), ksmvel@gmail.com (M. Kuppusamy), emmanueltoba90@gmail.com, oluwatoba.oyeneyin@aaua.edu.ng (O.E. Oyeneyin).

https://doi.org/10.1016/j.heliyon.2022.e10831
Received 18 August 2022; Received in revised form 8 September 2022; Accepted 26 September 2022

piperidin-4-one molecules normally acquire a chair conformation; however, the conformation may differ from the others depending on the phenyl ring substitutions [11, 12, 13, 14].

Their use as medicinal/pharmaceutical agents is well reported [15, 16]. Some of the derivatives have been reported for their ability to inhibit tuberculosis [17], influenza [18] and Severe Acute Respiratory Syndrome-Coronavirus Disease (SARS-COVID or SARS-CoV-2) [19,20]. With the outbreak of a new coronavirus in 2019 (COVID-19), there have been more than 281 million confirmed cases and about 5.4 million deaths recorded all over the world [21] as at the 3rd of January 2022. The devastating effects from this pandemic was felt by individuals, governments and businesses, this led to an urgent development of vaccines as no cure was found. As at the 3rd of January 2022, a total of 8.69 million vaccine doses have been administered [21]. However, with different controversies surrounding the use of vaccines [22], the search for drugs that can combat the disease is ongoing. Although, Veklury (remdesivir) has been approved by the United States of America's Food and Drug Administration (USA-FDA) [23], the World Health Organization (WHO) raised some reservations on its use for the treatment of COVID infections [24]. The main protease ($M_{pro}$) also known as the 3-Chromotrypsin-like protease ($3CL_{pro}$), RNA dependent RNA polymerase (RdRp), human Angiotensin-Converting Enzyme 2 (ACE-2) and Papain-like protease ($PL_{pro}$) are enzymes of coronaviruses [25, 26]. The $M_{pro}/3C_{pro}$ is crucial in polyprotein maturation process and therefore may serve as a therapeutic target in the search for SARS-CoV2 drugs [27, 28]. $PL_{pro}$ is very important in RNA virus polyproteins maturation and disruption of host immune responses [29]. SARS-CoV2 uses ACE-2 as an access into the host cell [30] while RdRp regulates viral replication [31]. Formulating antiviral drugs that can inhibit these enzymes is, therefore, very important in the development of effective SARS-CoV-2 drugs. In this regard, drugs like Baicalin, Baicalein and Perampanel analogue 5 have been reported to be effective against SARS-CoV-2 infection by inhibiting Mpro and $PL_{pro}$ activity via catalytic binding on the enzymes [31, 32, 33], Remdesivir has been approved by the FDA for its action against SARS-CoV-2 via its ability to inhibit RdRp [34, 35]. Angiotensin converting enzyme inhibitors (ACEIs) such as benazepril and angiotensin receptor blockers (ARBs) such as irbesartan were recommended for the treatment of SARS-CoV-2 infections by acting as ACE-2 inhibitors [36]. However, a lot of concerns have been raised with most of these drugs, from contraindications to disturbing side effects [37, 38], even with the FDA-approved remdesivir [39, 40]. Therefore, there is need to continually search for novel drugs that could combat SARS-CoV-2 effectively and safely.

Spectroscopic techniques like Fourier Transform Infrared (FT-IR), Nuclear Magnetic Resonance (NMR) and Mass Spectroscopy are helpful in establishing the structures of molecules [41, 42, 43, 44, 45]. Density Functional Theory (DFT) has been used solely and/or in conjunction with experimental methods for understanding the bonding and structural properties, characterization and applications of molecules [46, 47, 48, 49, 50]. Molecular docking helps to ascertain the interaction of molecules (ligands) with receptors and has been a useful technique in drug design and discovery [51, 52, 53, 54].

Spectroscopic application of organic systems has been associated with their structural features like asymmetric charge distribution, π-electron rich structure, donor-acceptor groups and low band gap [55, 56, 57, 58]. The distribution of charge density, localized atomic orbitals and electron localization which influence molecular stability, chemical reactivity and drug-like properties can be effectively studied using topological analyses such as atoms in molecule (AIM), molecular electrostatic potential (MESP), reduced density gradient (RDG), electron localization function (ELF) and localized orbital locator (LOL) maps [59, 60, 61, 62]. Similarly, biological and anti-COVID-19 investigations of drug candidates with benzoyl, benzoyloxy, carboxylate and pyridine moieties using in-vitro and in-silico approaches have been recently reported [63, 64, 65, 66, 67, 68] which motivates the present study of molecular and anti-SARS-CoV-2 properties of isopropyl 1-benzoyl-4-(benzoyloxy)-2, 6-diphenyl-1,2,5,6-tetrahydropyridine-3-carboxylate (IDPC). Therefore, this work reports the synthesis, characterization, topological (AIM, RDG, ELF, LOL and MESP) analysis and DFT calculations on the structural properties of IDPC. The inhibitory potentials of IDPC against SARS-COV-2 enzymes were also investigated via extra precision (XP) molecular docking technique.

## 2. Synthesis of IDPC [Scheme 1]

IDPC was synthesized by Mannich condensation of benzaldehyde with isopropyl acetoacetate. 0.01 mol of Isopropyl acetoacetate, 0.02 mol of benzaldehyde and 0.01 mol of ammonium acetate were put in a round bottom flask (500 ml). Ethanol was added (25 ml), warmed for about 10 min and allowed to crystallize. The product was filtered, with the solid product recovered, washed (cold water), dried (25 °C) and recrystallized from ethanol/ether to give 3-isopropyl-2,6-diphenylpiperidin-4-one carboxylate (3-IDC). A mixture of 3-IDC (3.37 g, 100 mmol) and benzoyl chloride (2 ml, 100 mmol) triethylamine (2 ml, 200 mmol) and benzene (50 ml) was refluxed for 6 h under monitoring with TLC. The solvent was washed with 2 *M hydrochloric* acid (10 ml) followed by water. Solvent was removed under vacuum and the residue was recrystallized from ethanol. Yield of product was 2.65 g (70%) [69].

**FTIR ($cm^{-1}$) (KBr)**: 1731, 1708, 1700 $cm^{-1}$ [carbonyl groups and one amide carbonyl group], 1708 $cm^{-1}$ [ester carbonyl of hydroxyl group, C-4], 1731 $cm^{-1}$ [ester carbonyl group, C-3], 1700 $cm^{-1}$ [amide carbonyl group], 1640 $cm^{-1}$ [aromatic C=C stretch] (Table S1); **$^1$H NMR ($CDCl_3$)**: 6.83–8.11 [aromatic protons, m], 0.61, 0.99 [methyl protons of COOiPr at C-2, d, d (6.3)], 4.76 [methine protons of COOiPr at C-2, m], 6.89 [$H_{5a,}$ m], 3.12 ($H_{5e,}$ d (18.3)), 2.99 [$H_{5a,}$ dd (7.2, 2.1)], 5.7 [$H_{2a,}$ broad]; **$^{13}$C NMR ($CDCl_3$)**: 126.3–137.8 [aromatic carbons], 164.5 [ester carbonyl at C-4], 171.4, 68.5, 21.4, 20.98 [CO, methine and methyl groups of COOiPr at C-2], 56.4 [C-6], 31.4 [C-5], 138.7 [C-4], 120.1 [C-3], 53 [C-2].

### 2.1. Spectral characterization

FT-IR details of the IDPC was recorded in the region of 4000–400 $cm^{-1}$ on AVATAR 330 FTIR Thermo Nicolet Spectrometer in KBr pellets at Annamalai University, Annamalai Nagar, Tamil Nadu, India. 1D and 2D NMR spectra were recorded on a Bruker AV 300 NMR spectrometer operating at 300.13 MHz for $^1$H and 75.47 MHz for $^{13}$C. For $^1$H NMR spectrum, 10 mg of IDPC was dissolved in 0.5 ml of $CDCl_3$. For recording 2D spectra 50 ml of IDPC was dissolved in 0.5 ml of $CDCl_3$. X-ray crystallography analysis confirmed the structure of the compound [69].

## 3. Computational details

IDPC was optimized with DFT method at the B3LYP/6–311++G (d,p) level of theory [70] with Gaussian 09 software [71] with the aid of the Chemcraft visualization program [72]. The nature and types of H-bonding were examined with atoms in molecule (AIM), electron localization function (ELF), localized orbital locator (LOL) and reduced density gradient (RDG) analysis using Multiwfn software [73]. The isosurface maps were visualized using VMD software package [74]. The reactivity of the title molecule was predicted by using the energy gap

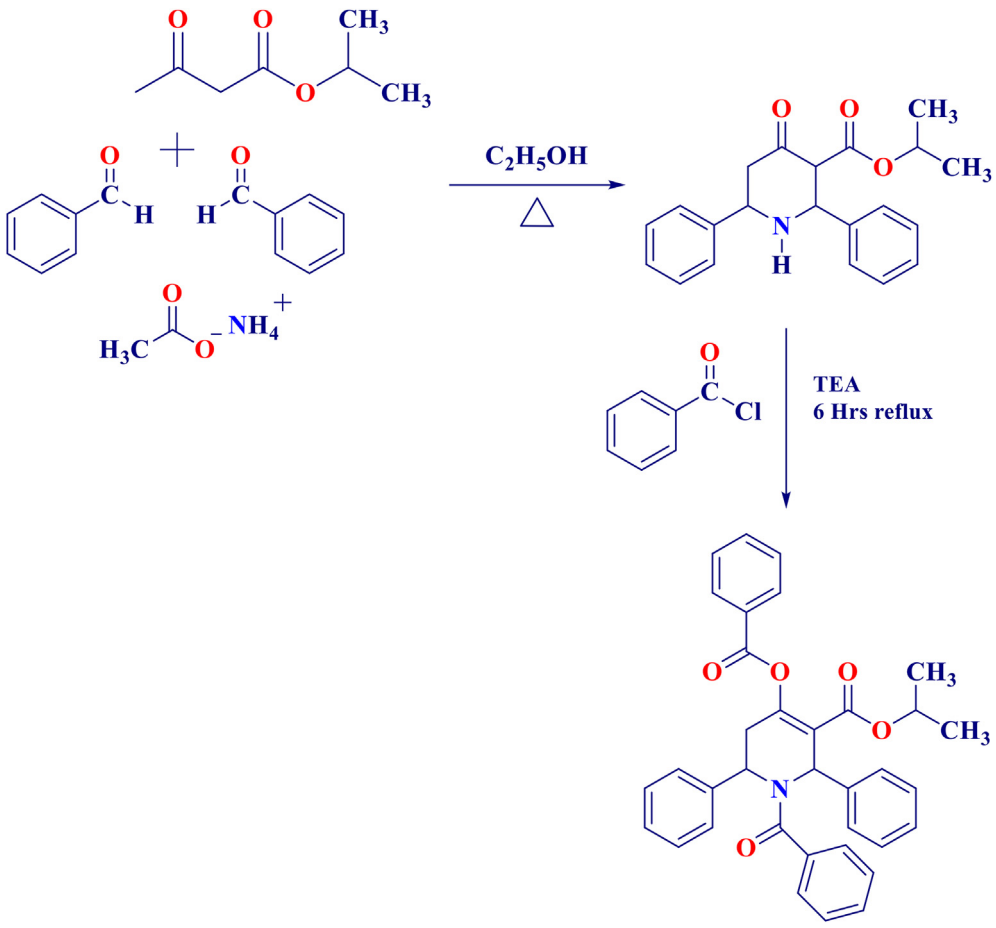


**Scheme 1.** Synthetic Scheme of IDPC.

between the HOMO and LUMO orbitals via DFT approach [75]. Further, the molecular electrostatic potential map (MESP) surface has been computed at the same level of theory using GaussView [76]. IDPC was docked into the active sites of SARS COVID-19 Mpro, 6W63 (resolutions 2.10 Å), PLpro, 7JRN (resolution 2.48 Å), RdRp receptor, 7BV2 (resolution 2.50 Å) and ACE2 receptor, 6M18 (resolution 2.90 Å). The receptors were downloaded from the Protein Data Bank website [77]. The co-crystallized ligands accompanying the receptors were re-docked for docking validation and for comparison. The receptors and IDPC were prepared using the Protein Preparation Wizard and LigPrep, respectively in the Maestro/Schrodinger suite [78, 79]. The site maps were generated [80] before extra precision (XP) docking of the compounds and co-crystallized ligands in the active sites of the receptors (6W63: x = -20.71, y = -16.36, z = -27.59; 7JRN: x = 9.99, y = -10.18, z = 31.72; 7BV2: x = 106.81, y = 111.26, z = 99.09; 6M18: x = 127.74, y = 127.33, z = 135.64) using Glide [81].

## 4. Results and discussion

### 4.1. Assignment of proton and $^{13}C$ signals

In the $^{1}H$ NMR spectrum, as expected two doublets and one multiplet for isopropyl moiety of an ester group observed at 0.61, 0.89 and 4.76 ppm, and they are conveniently assigned to isopropyl group (Fig. S1). Two doublet of doublets at 2.98 and 3.12 ppm with coupling constant 7.2 Hz and 18 Hz are assigned to methylene protons at C-5 and it was confirmed by HOMOCOSY spectrum. Also, coupling between the two methyl protons (δ 0.61 and 0.89 ppm) and the methine proton of the isopropyl was observed as cross peaks in the $^{1}H$–$^{1}H$ COSY spectrum. The signals due to benzylic protons at C-2/C-6 are broadened and deshielded as a result of restricted rotation about N–C=O bond. Thus, the more deshielded broad signal 6.89 ppm was assigned to H-6 proton, while the other at 5.7 ppm due to H-2 protons.

Individual carbon signals were assigned with the help of DEPT-135 and HSQC spectra. In the $^{13}C$ NMR spectrum, signals observed at 171.4, 164.5, 162.7, 138.8, 137.8, 136.5, 129.0 and 120.1 ppm are assigned to quaternary carbons, which is confirmed by DEPT spectrum The above signals are missing in the DEPT spectrum. In the above, the C-13 signals at 171.4, 164.5 and 162.7 ppm are assigned conveniently to the ester carbonyl at C-3, C-4 and amide carbonyl groups, respectively. C-13 signals at 138.8 and 120.1 ppm are assigned to C-4 and C-3 respectively based on similar reported values [82].

Remaining quaternary signals are due to ipso carbons of the phenyl groups at C-2, C-6 and benzoyl group. In the HSQC spectrum, cross peaks 2.98/31.4 and 3.15/31.4 shows the correlation between methylenic protons with C-5. Hence the C-13 signal at 31.4 ppm is unambiguously assigned to C-5. C-13 signals at 20.9, 21.4 and 68.4 ppm are due to isopropyl group of the ester at C-3. The cross peak at 5.7/53.0 and 6.7/54.6

reveals the correlation between H-2 proton with C-2 and H-6 with C-6. Hence the C-13 resonance at 53.0 and 54.6 ppm are assigned to C-2 and C-6. Other C-13 resonances from 126.3 to 133.9 ppm are assigned to aromatic carbons (see Supplementary Information, Figs. S2 – S5).

### 4.2. Conformation analysis

The introduction of the benzoyl group to heterocyclic nitrogen can adopt either a coplanar or perpendicular orientation to the reference plane of the piperidine ring system [83, 84]. π-electron orbital of the amide carbonyl group overlaps with the orbital of the lone pair of electrons on the nitrogen thereby stabilizing the planar conformation. Also, the benzylic protons are broadened instead of getting splitting in their signals as observed in the parent piperidone. This suggests the existence of limited rotation about N–C=O group brought about by high energy barrier. Despite this, only one set of signals for the ring proton was observed instead of two set of signals corresponding to two rotamers Figure 1 arising out of limited rotation [82, 83]. In IDPC, benzylic proton at C-2 shows a broad signal while benzylic proton at C-6 merged with aromatic protons (refer proton NMR spectrum). Ring methylene protons at C-5 appear as doublet of doublet.

By comparing the parent piperidone with substituted nitrogen in the heterocyclic ring makes the ring protons to de-shield significantly. By comparing the coupling constant of parent wit N-substituted compound more substituted rigid chair conformation is not possible. Therefore, it is noteworthy that the decreased coupling constant value in IDPC may be due to increased electronegativity of nitrogen. Thus, IDPC exists in equilibrium between half boat conformations as seen in Figure 1.

### 4.3. Optimized parameters

The structure of IDPC optimized with DFT method at the B3LYP/6–311++G (d,p) level of theory is presented (Figure 2). The geometric parameters (bond lengths and angles) were obtained. The experimental bond lengths and angles from X-ray analysis [63] were compared with those obtained with DFT calculation. There is a close agreement between them (Table S2). This infers that DFT calculations can be used for structural elucidation of hypothetical molecules prior synthesis.

### 4.4. Atoms in molecule (AIM) analysis

The "atoms in molecules" (AIM) is a quantum chemistry model for characterizing the chemical bond of a system based on a topological charge density approach. This method gives the information about the presence of strong and weak hydrogen bonds. This analysis of electron density (ρ) at different characteristic points is developed by Bader [85, 86]. So, to understand the non-covalent interactions existing within the studied molecule, AIM analysis was performed. This analysis was used to search all the bond critical points (BCP) using Multiwfn software [73] and the geometrical structure is shown [Figure 3]. From the AIM method, the energetic, geometrical and topological parameters are determined here as descriptors of hydrogen bonding proprieties. Table 1 summarized the calculated values obtained at BCP for IDPC. The electron density ρ(r), its Laplacian $\nabla^2\rho(r)$, kinetic energy density G(r), potential V(r), total energy density H(r) and the total energy E interactions are used to measure the strength and the nature of the bond at BCPs [87]. In addition, the topological parameters $\nabla 2\rho(r)$, H(r) and the ratio |V|/G allows to classify the nature of the chemical interactions into three types [88]: when the $\nabla 2\rho(r) > 0$, $H(r) < 0$ and $|V|/G > 2$, the type of interaction is shared-shared (SS), covalent. The type shared-closed (SC), transit or

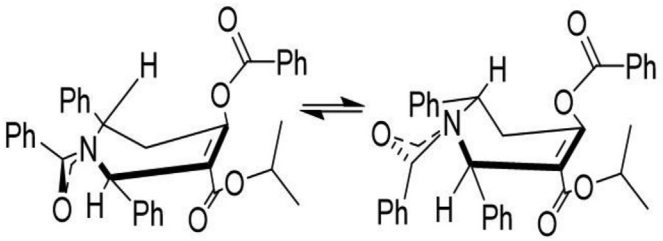


**Figure 1.** IDPC molecule occurs in a state of equilibrium between half boat conformations.

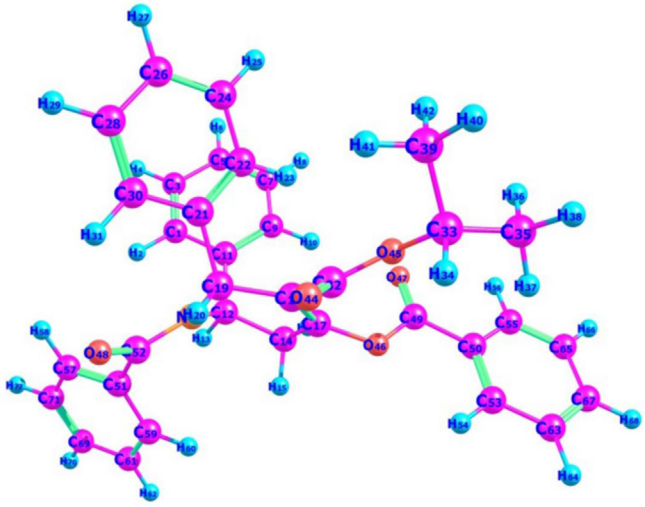

**Figure 2.** Optimized structure of IDPC.

intermediate is indicated by $\nabla 2\rho(r) > 0$, $H(r) < 0$ and $1 < |V|/G < 2$. Whereas for $\nabla 2\rho(r) > 0$, $H(r) < 0$ and $|V|/G < 1$, the interaction is closed-closed (CC), ionic, van der Waals... Inspection of the Table indicates that the Laplacians $\nabla 2\rho(r)$ and the total energy densities H(r) of all interactions are positive. The ratios $|V|/G < 1$ in all cases, indicating a pure ionic, van der Waals interactions (CC). The values of energy interactions of the C–H···O types are less than 50 kJ/mol (12 kcal/mol). These results prove that the hydrogen bonds existing within IDPC are considered weak.

### 4.5. Reduced density gradient (RDG) analysis

The reduced density gradient (Eq. 1) is derived from the first derivative of the density. The RDG and its first derivative *S*, describes the deviation from a homogenous electron distribution [89].

$$\mathrm{RDG(r)}\ \ S = \frac{1}{2(3\pi^2)^{1/3}} + \frac{|\nabla\rho(r)|}{\rho(r)^{4/3}} \quad (1)$$

It is used to identify covalent bonds and other non-covalent interactions by plotting ρ(r) against sign $\lambda_2$. Non-bonding interactions occur when $\lambda_2$ is positive while bonding interactions occur when $\lambda_2$ is negative. The top of the plot indicates strong interaction while the bottom indicates weak interaction of the molecular system. The RDG analysis here was performed using Multiwfn 3.7 software [73]. The interactions represented via RDG isosurface enclosing their real space,

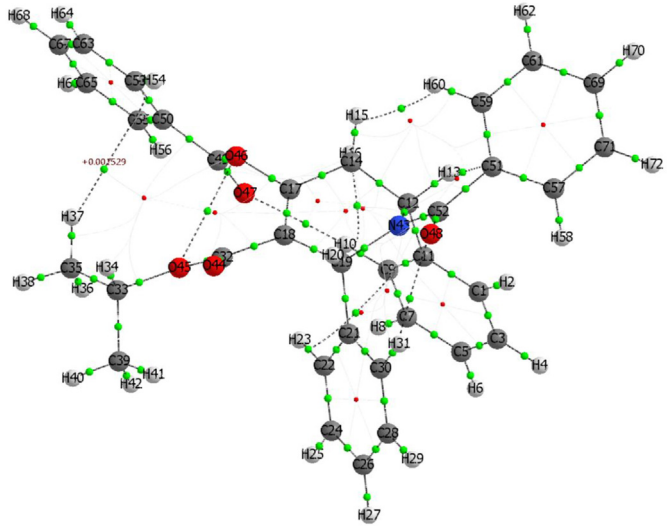

**Figure 3.** AIM representation of bond critical points within the IDPC.

where the hydrogen bond interactions, vdW interactions and steric effect are represented by the blue, green and red regions, respectively (Figs. 4a and b). In Figure 4a, the red regions at the centre of the three aromatic rings indicate the effect of steric repulsion in IDPC while the green colour isosurface represents non-covalent interactions. The intermolecular distance of 2.65Å has about 31% from the Hirshfeld surface and it is consistent with H...π interactions. The blue colour in the RDG isosurface indicates the strong attraction of IDPC. The RDG, hence, predicts the possible H-bonding, covalent and non-covalent interactions between the IDPC and SARS-COVID receptors mainly via the π-bonds and the heteroatoms.

### 4.6. ELF and LOL maps

The Electron Localization Function (ELF) and Localized Orbital Locator (LOL) topological analyses were employed in rationalizing the chemical content of the molecule. Their values usually range between 0 and 1. The red colour legend indicates the upper limit values close to 1; white indicates values that exceed the upper limit; black depicts values below the lower limit; and blue indicates values below 0.5. Values of ELF close to unity indicates great localization of electron suggesting a nonbonding electron pair, covalent bond or inner shells of the atom involved while values <0.5 depict electron delocalization [90, 91]. The LOL also explains the localization of orbitals, where small LOL value essentially appears at the boundary region and large values appear at the inner region of the localized orbitals. The colour-shaded ELF and LOL maps of IDPC are reported in Figure 5(a) and (b), respectively. The red region around the hydrogen atoms in the ELF and LOL maps indicates high electron localization due to covalent bond or lone-pair of electrons while the light blue and deep blue colour in the inner regions of the nitrogen (N43) and phenyl carbon atoms signifies remarkable delocalization of electron cloud [90]. Additional information about the localization of atomic orbitals was obtained for the hydrogen and carbon atoms in the LOL topological analysis. In the LOL map, the inner white region in the H orbitals (H27, H54, H62 and H64) indicates that the electron density in that region exceeds the upper boundary of the colour legend [92]. Also, significant localization of bonding orbitals was observed between the $sp^2$-hybridized carbon atoms (for instance, C61 and C69), indicating well-localized covalently bonded orbitals.

### 4.7. Global reactivity descriptors and electrostatic potential (MESP) maps

The electrostatic interactions and the reactivity of IDPC were obtained from the frontier molecular orbitals ($E_{HOMO}$ and $E_{LUMO}$) [93]. The HOMO of IDPC is distributed over the 2,6-diphenyl moiety to the tetrahydropyridine group, with an energy of -2.04 eV while the LUMO is distributed across the benzoyl ring, with an energy of -6.51 eV, making the energy band gap (ΔE) of IDPC to be 4.47 eV (Figure 6). It shows that there is intramolecular charge transfer within the molecule. Other properties (reactivity descriptors) are presented (Table 2), with chemical hardness, softness, chemical potential and global electrophilicity being 2.235, 0.224, -4.275 and 4.089 eV respectively. The global electrophilicity gives us the electron flow between donor-acceptor species. The high electrophilicity index value of 4.089 eV shows that the IDPC will act as an electrophile in biological responses. The chemical hardness value 2.235 eV for IDPC reveals that the molecule is not as hard as benzene whose chemical hardness is 3.2943 eV [59]. The molecular electrostatic potential (MESP) map shows the electrophilic and nucleophilic regions on the molecular structure as a result of asymmetric charge distribution [94]. The red region is the highly negative electrostatic potential surface depicting areas where a positive charge (electrophile) will likely attack while the blue region (positive electrostatic potential) is the local reactive site that is susceptible to nucleophilic attack (Figure 7) [95]. Highly negative electrostatic potential is essentially localized around the oxygen of carbonyl groups of the benzoyl, benzoyloxy and isopropyl carboxylate moieties indicating that they are local nucleophilic sites. The yellow map on the phenyl rings indicates their negative electrostatic potential and possible π-π stacking interactions with the receptor's aromatic active sites. The electrophilic centres (positive electrostatic potentials) are located mainly over the phenyl hydrogen. The hydropyridinyl nitrogen is relatively electrostatically neutral indicating that it may not be involved in either nucleophilic or electrophilic attack. The MESP, therefore, indicates the carbonyl oxygen as

**Table 1.** Calculated topological parameters of IDPC.

| Interactions types | $\nabla^2\rho(r)$ (a.u) | ρ (r) (a.u) | G(r) (a.u) | V(r) (a.u) | H(r) (a.u) | ε | $E_{interactions}$ kJ/mol |
|---|---|---|---|---|---|---|---|
| $C_{30}$–$H_{31}$...$O_{48}$ | 0.0349 | 0.0107 | 0.0077 | -0.0066 | 0.0011 | 0.0732 | -8.66 |
| $C_9$–$H_{10}$...$O_{47}$ | 0.0332 | 0.0102 | 0.0071 | -0.0059 | 0.0012 | 0.0279 | -7.75 |
| $C_9$–$H_{10}$...$OH_{16}$ | 0.0495 | 0.0121 | 0.0100 | -0.0077 | 0.0023 | 1.4900 | -10.11 |
| $C_{33}$–$O_{45}$...$O_{46}$ | 0.0475 | 0.0117 | 0.0106 | -0.0092 | 0.0014 | 0.8222 | -12.08 |
| $C_{35}$–$H_{37}$...$C_{53}$ | 0.0075 | 0.0028 | 0.0015 | -0.0012 | 0.0003 | 1.1146 | -1.58 |
| $C_{14}$–$H_{15}$...$H_{60}$ | 0.0137 | 0.0043 | 0.0028 | -0.0022 | 0.0006 | 0.6896 | -2.89 |
| $C_{12}$–$H_{13}$...$C_{51}$ | 0.0567 | 0.0159 | 0.0121 | -0.0100 | 0.0021 | 1.8909 | -13.13 |

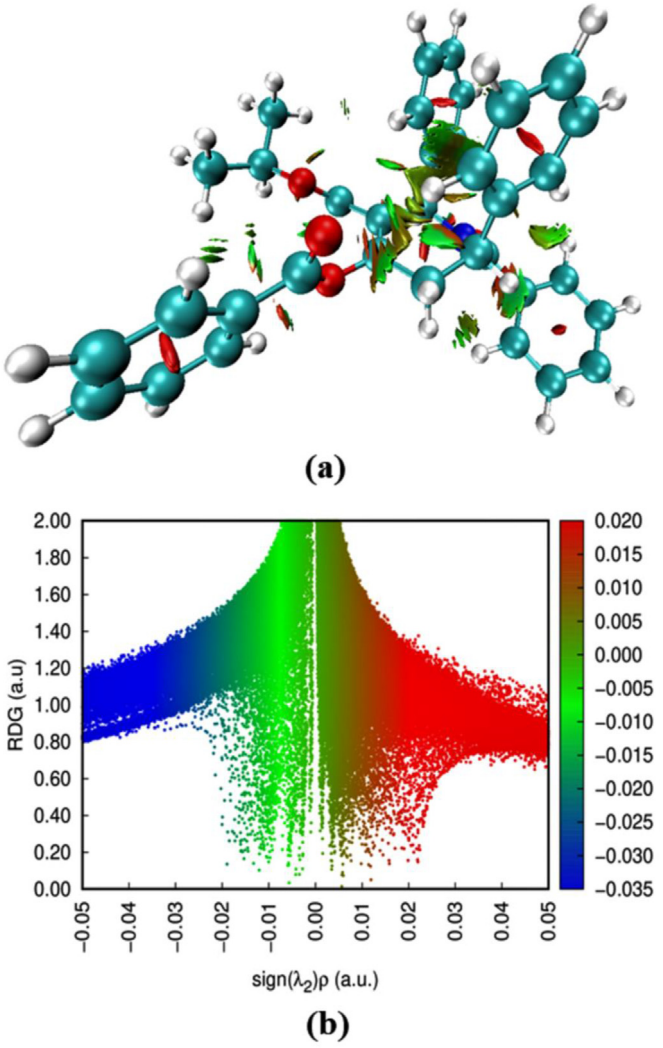


**Figure 4.** (a) RDG graph and (b) RDG scatter map of the IDPC where the hydrogen bond interactions, vdW interactions and steric effect are represented by the blue, green and red regions, respectively.

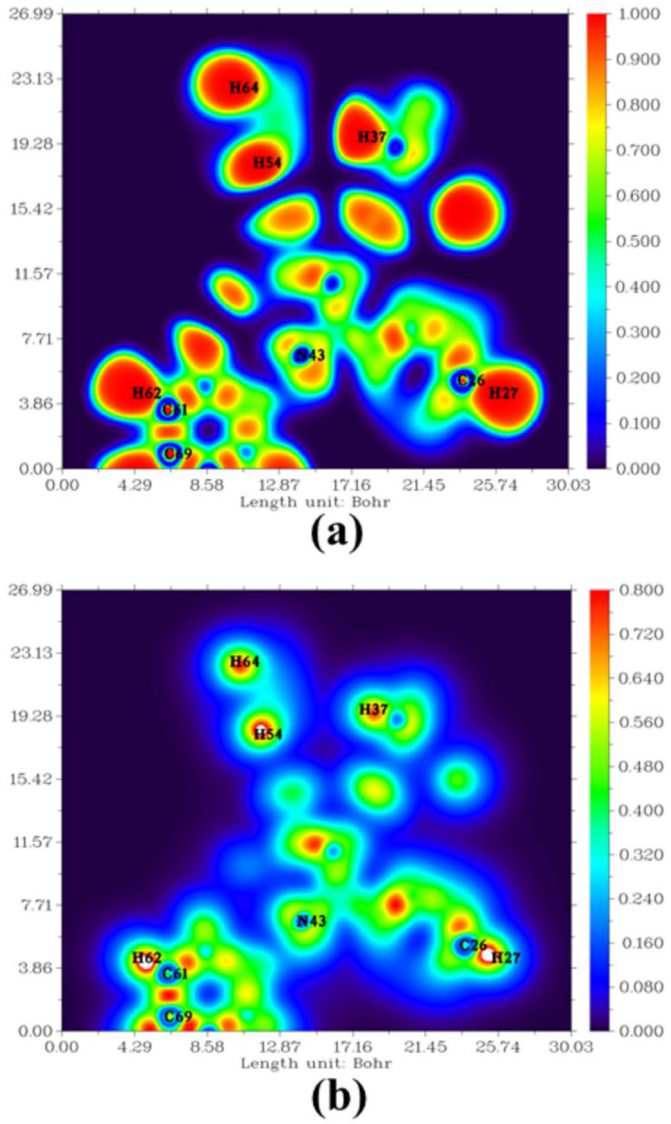


**Figure 5.** (a) ELF and (b) LOL maps of the IDPC.

the local binding site for possible interactions with the electrophilic regions (active sites) of the SARS-COVID receptors.

### 4.8. Vibrational assignments

The theoretical vibrational analysis of IDPC was conducted at DFT/B3LYP/6–311++G (d,p) level of theory. The absence of imaginary frequency in the vibrational modes confirms that the optimized geometry corresponds to a minimum [96]. Since a molecule of IDPC is a nonlinear polyatomic system with 72 atoms, 210 normal vibrational modes were obtained. The calculated IR and Raman spectra are depicted in Figure 8 with pure Lorentzian band shape. The computed wavenumbers, scaled frequency and their intensity of IR and Raman data are compared and listed in Table S3. The IR frequencies were corrected using scaled quantum mechanics (SQM) for good comparison with experimental data (Table S3) [97]. The vibrational frequencies were scaled by 0.983 and 0.958 for wavenumbers 4000–1700 and <1700 $cm^{-1}$, respectively [98, 99]. Although there is a difference in intensity between the normal vibrational modes, a good agreement is observed between the calculated vibrational frequencies of the IR and the Raman spectra. The computed vibrational modes aid the assignment of the characteristic vibration like C–H, C=O, C–O and C=C bonds. These essential normal vibrational modes of IDPC are both IR- and Raman-active though with different intensities, indicating their change in dipole moment and polarizability on absorption of appropriate energy [100, 101]. The vibrational frequencies between

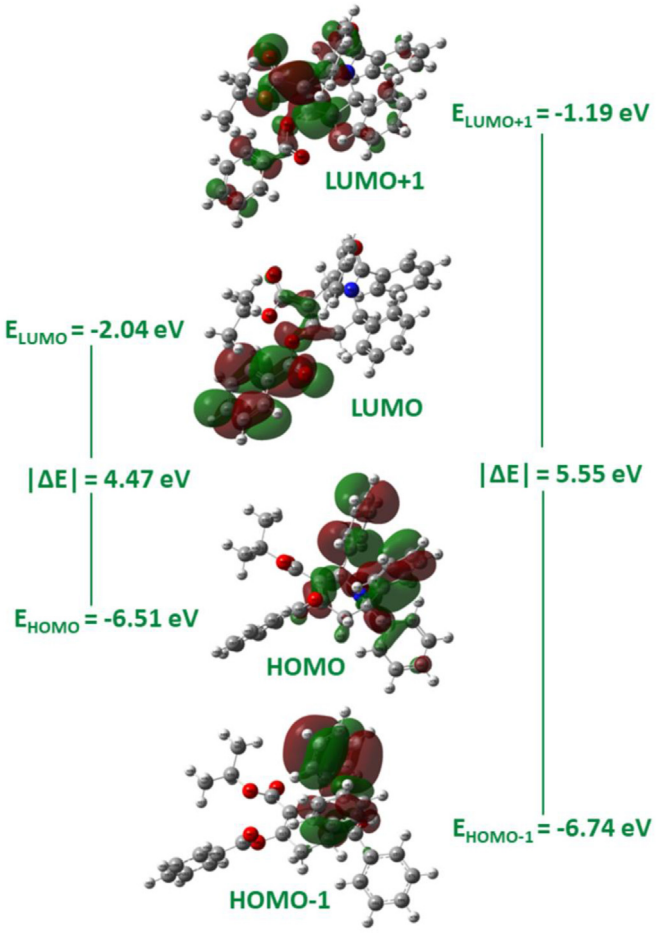


**Figure 6.** Frontier molecular orbital's image of IDPC.

**Table 2.** The frontier molecular orbitals of IDPC.

| Quantum Parameters | DFT/B3LYP/6–31++G (d, p) |
|---|---|
| $E_{HOMO}$ (eV) | -6.51 |
| $E_{LUMO}$ (eV) | -2.04 |
| $E_{HOMO+1}$ (eV) | -6.74 |
| $E_{LUMO-1}$ (eV) | -1.19 |
| $\Delta E_{HOMO-LUMO}$ (eV) | 4.47 |
| $\Delta E_{HOMO-1-LUMO+1}$ (eV) | 5.55 |
| I | 6.51 |
| A | 2.04 |
| χ | 4.28 |
| η | 2.24 |
| μ | -4.28 |
| ω | 4.09 |
| S | 0.22 |

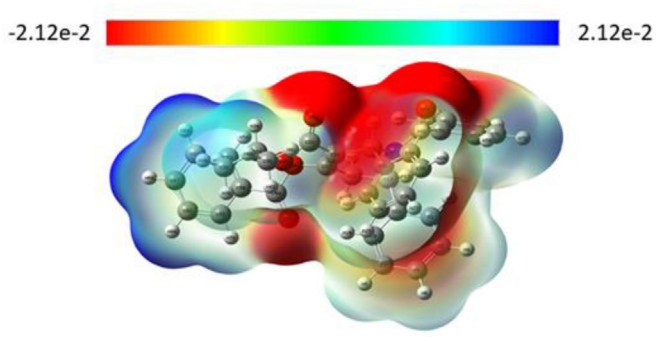


**Figure 7.** Molecular electrostatic surface of the IDPC.

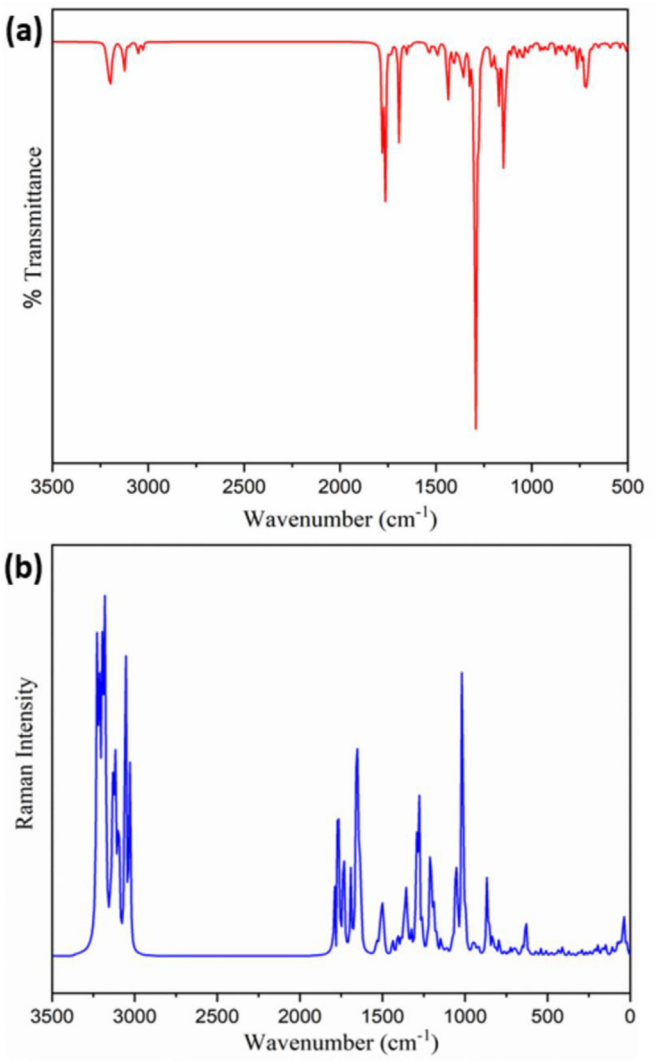


**Figure 8.** Theoritical **(a)** IR and **(b)** Raman spectra of the IDPC compound.

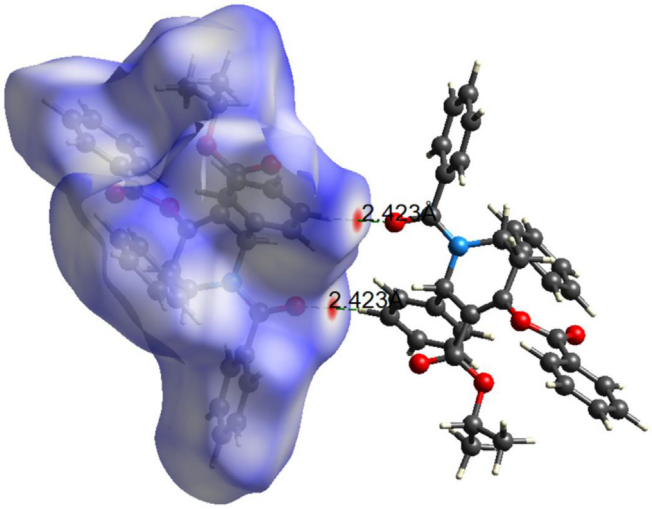


**Figure 9.** Hirshfeld analysis mapped with $d_{norm}$ and showing adjacent molecule outside the surface for the IDPC.

2978 – 3175 $cm^{-1}$ are assigned the C–H stretch. The C=O stretching vibration is easy to assign as it usually appears around 1700 $cm^{-1}$. The three C=O stretching vibrations observed at 1749, 1735 and 1706 $cm^{-1}$ could be assigned to the carbonyl groups of the benzoyloxy, isopropyl carboxylate and benzoyl moieties. The C–O stretch of the ester functional was obtained at 1122, 1098, 1034 and 915 $cm^{-1}$. The aromatic C=C stretch was observed over a range of vibrational frequencies (for instance, 1609, 1607 and 1605 $cm^{-1}$). The computed and the experimental wavenumbers are in good agreement (see Supplementary Information, Fig. S6).

### 4.9. Hirshfeld surface analysis

Hirshfeld surface analysis produces an excellent graphical depiction. Hirshfeld's surface and fingerprint plots are suitable for analysing the inputs of neighbouring atoms' interactions and the precision of molecular structure [102, 103]. Hirshfeld surfaces (HS) were generated using Crystal Explorer 17.5 software to illustrate the critical interactions inside the crystal of the IDPC molecule. Hirshfeld analysis for the IDPC utilizing the $d_{norm}$ with an adjacent molecule beyond the surface, as illustrated in Figure 9. The red region represents the more prominent interaction between oxygen (O) and hydrogen (H) atoms [49]. Also, C–C and H–H interactions are seen on the Hirshfeld surfaces. Hirshfeld surfaces for $d_i$, $d_e$, $d_{norm}$, shape index, and curvedness of IDPC compound were illustrated in Figure 10. The intramolecular diameter of the closest nucleus from the point beyond the region of surface values ranges from -0.1327 to 2.5293. The normalized distance of the title structure's contact surface $d_{norm}$ value is between -0.1327 and 1.5982. The red areas on the $d_i$ and $d_e$ surfaces of the IDPC molecule represent $\pi$...C–H interactions. The interatomic interactions engaged in the high hydrogen bonding and interatomic interactions are depicted by the red patch on the surface. The IDPC molecule has intermolecular hydrogen bonding, resulting in a red colour spot area on the $d_{norm}$ diagram. The 2D fingerprint plots in Figure 11(i) depict the title molecule's 100 percent weak intermolecular interactions ($d_i$ Vs $d_e$). Figure 11(ii) depicted the 2D Fingerprint plots of the major intercontact and proportion of various intermolecular interactions contributed to the Hirshfeld surfaces. (*a*) H···H (63.1 %), (*b*) C···H/H···C (18.3 %), (*c*) H···O/O···H (13.5 %), (*d*) C···C (3.1 %), (*e*) O···C/C···O (1.2 %) and (*f*) O···O (0.8 %) in IDPC compound.

### 4.10. Molecular docking discussion

IDPC was docked against four SARS-COVID (Mpro, PLpro, ACE2 and RdRp) receptors, with binding affinities recorded (Table 3). For the Mpro receptor 6W63, IDPC had higher binding affinity (–6.966 kcal $mol^{-1}$ for 6W63) than the co-crystallized ligand (−6.722 kcal $mol^{-1}$). IDPC showed a pi-cationic interaction with HIP via its phenyl ring and hydrogen bond interaction with GLN 189 via its carbonyl oxygen group (Figure 12a) while its co-crystallized ligand (X77) showed hydrogen bond interactions with ASN 142 (via carbonyl oxygen), GLU 166 (via carbonyl oxygen) and THR 25 via its amino hydrogen (Figure 12b). The compounds showed

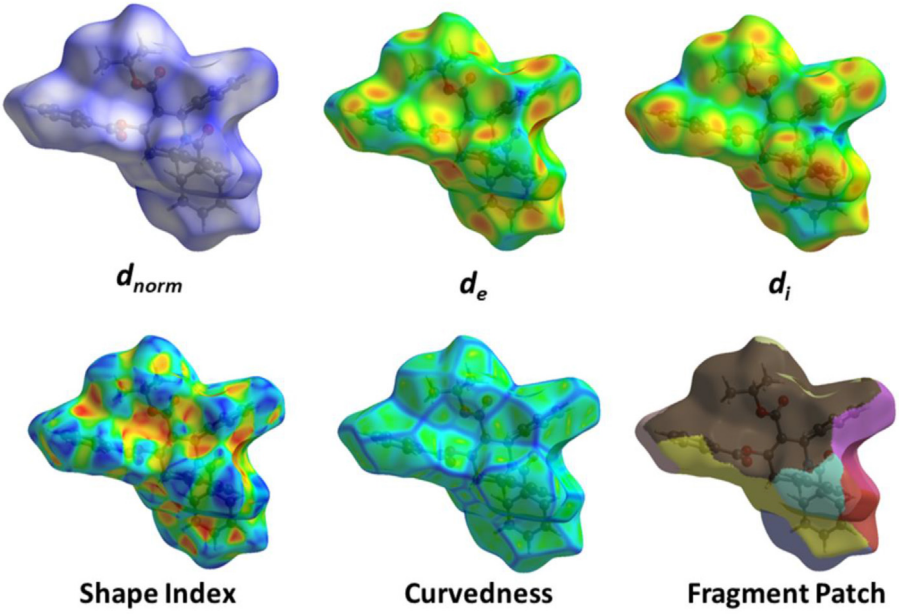


**Figure 10.** Hirshfeld surface for IDPC with $d_i$, $d_e$, $d_{norm}$, shape index, curvedness and fragment patch.

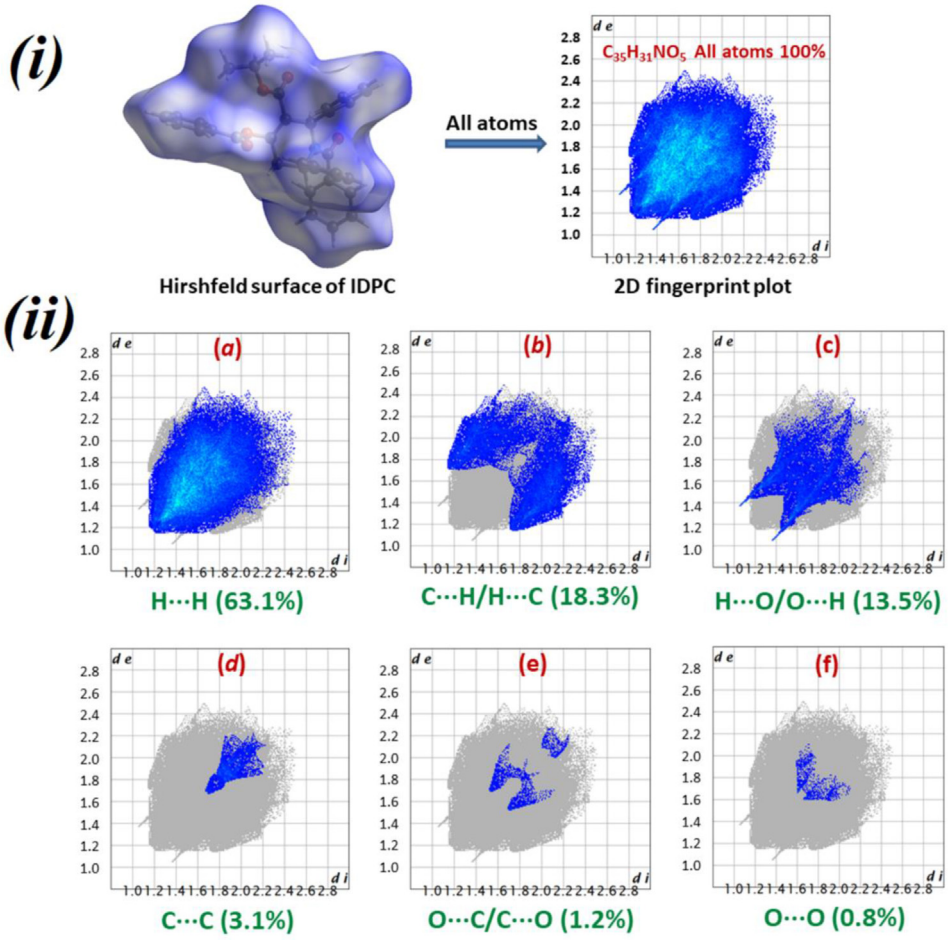


**Figure 11.** (i) 2D fingerprint plots of the Hirshfeld surface contact contributing 100 percent of IDPC (ii) 2D Fingerprint plots of the significant intercontact and percentage of various intermolecular contacts contributed to the Hirshfeld surfaces (*a*) H···H (63.1 %), (*b*) C···H/H···C (18.3 %), (*c*) H···O/O···H (13.5 %), (*d*) C···C (3.1 %), (*e*) O···C/C···O (1.2 %) and (*f*) O···O (0.8 %) in IDPC compound.

**Table 3.** Docking results of IDPC molecule and various SARS-COVID receptors, as well as their co-crystallized compounds.

| Receptor type | Receptors | Molecule | XP Docking score (kcalmol$^{-1}$) |
|---|---|---|---|
| Mpro | 6W63 | IDPC | -6.966 |
| | | Co-ligand | -6.722 |
| | | 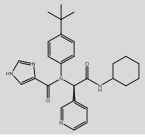 | |
| PLpro | 7JRN | IDPC | -4.141 |
| | | Co-ligand | -6.915 |
| | | 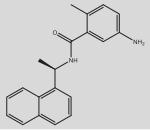 | |
| RdRp | 7BV2 | IDPC | -4.847 |
| | | Co-ligand | -5.396 |
| | | 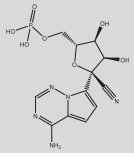 | |

(*continued on next page*)

**Table 3** (*continued*)

| Receptor type | Receptors | Molecule | XP Docking score (kcalmol$^{-1}$) |
|---|---|---|---|
| ACE2 | 6M18 | IDPC | -3.658 |
| | | Co-ligand 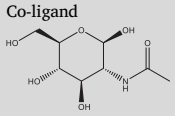 | -4.933 |

hydrogen bond interaction with the receptors, this was also observed in previous work [25, 104].

For the PLpro receptor, 7JRN, IDPC had binding affinity lower (−4.141 kcal mol$^{-1}$) than the co-crystallized ligand (−6.915 kcal mol$^{-1}$). IDPC showed a pi-pi stacking interaction with TYR 268 via its phenyl ring, hydrogen bond interactions with TYR 268 and ARG 166 via its carbonyl oxygen groups (Figure 13a) while its co-crystallized ligand (TTT) showed hydrogen bond interaction with GLN 269 via its carbonyl oxygen, pi-pi stacking interactions with TYR 268 via its naphthalene and benzamide rings (Figure 13b).

For RdRp receptor (7BV2), IDPC had a lower binding affinity of -4.847 kcal mol$^{-1}$ than the co-crystallized ligand, F86 (−5.396 kcal mol$^{-1}$). IDPC showed a pi-cationic interaction with ARG 349 via its phenyl ring, hydrogen bond interactions with ARG 349 and PHE 396 via its carbonyl oxygen groups (Figure 14a) while its co-crystallized ligand (F86) showed hydrogen bond interactions with PHE 396, VAL 675, GLU 350 and ARG 349 via its hydroxyl and amino hydrogen groups and a salt bridge with ARG 349 via its phosphate oxygen (Figure 14b). The formation of hydrogen bond and pi-cationic interactions was also observed in the work of Gajjar *et al* [104] and Singh *et al* [105].

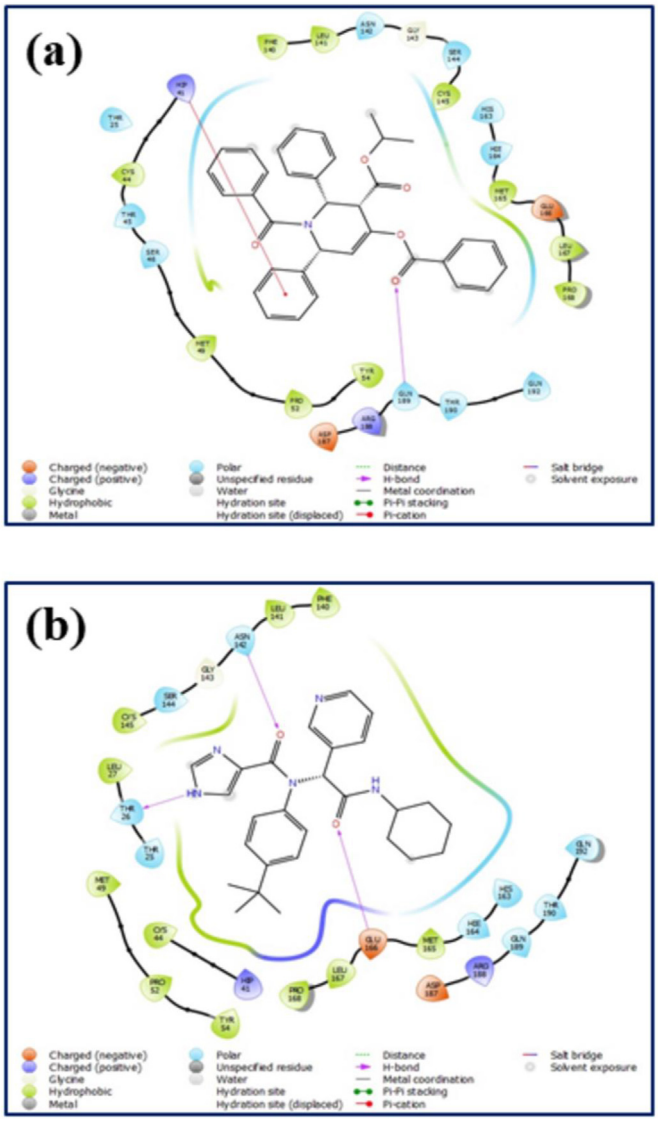


**Figure 12.** Docking interactions with 6W63 (a) IDPC (b) Co-ligand N-(4-tert-butylphenyl)-N-[(1R)-2-(cyclohexylamino)-2-oxo-1-(pyridin-3-yl)ethyl]-1H-imidazole-4-carboxamide (X77).

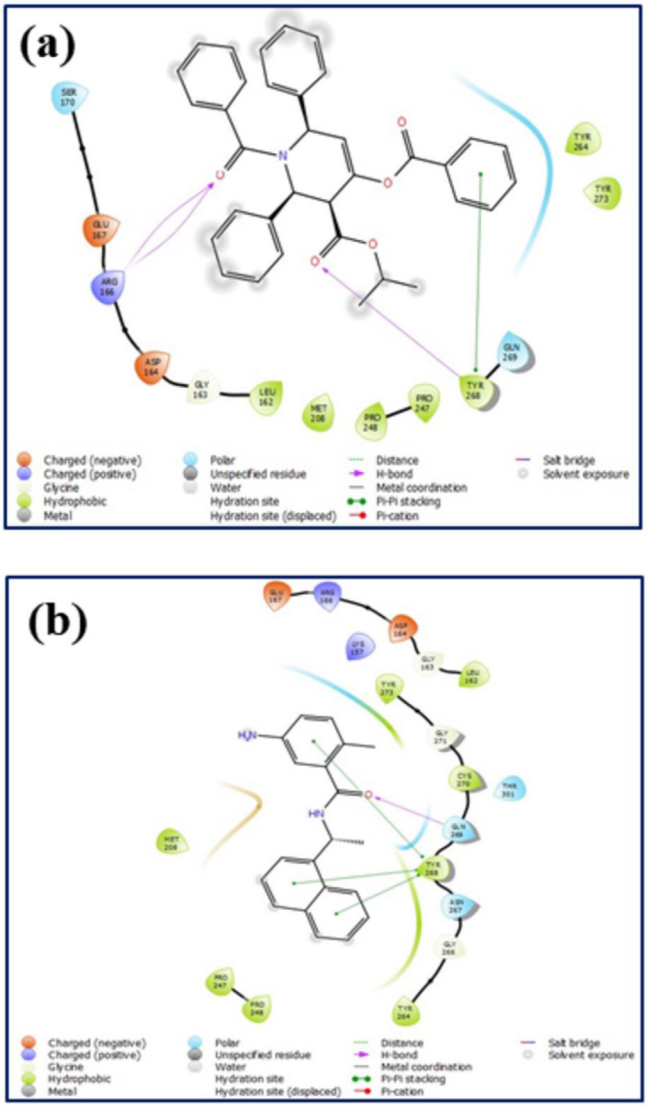


**Figure 13.** Docking interactions with 7JRN (a) IDPC (b) Co-ligand, 5-amino-2-methyl-N-[(1R)-1-naphthalen-1-ylethyl]benzamide (TTT).

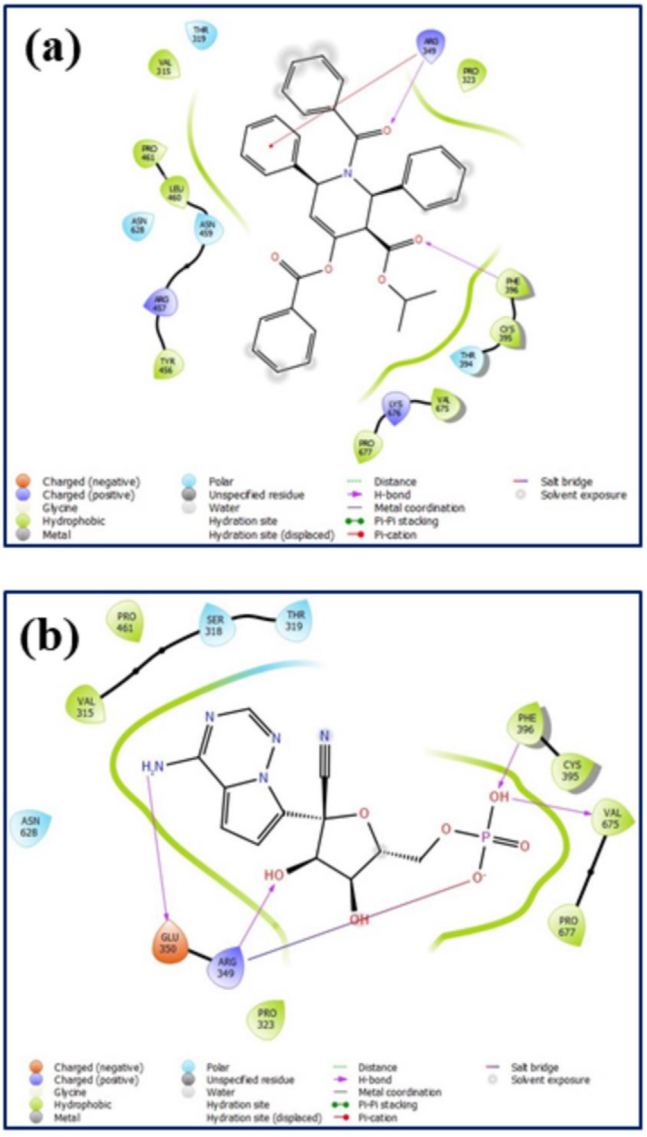


**Figure 14.** Docking interactions with 7VB2 (a) IDPC (b) Co-ligand, [(2~{R},3~{S},4~{R},5~{R})-5-(4-azanylpyrrolo [2,1-f][1,2,4]triazin-7-yl)-5-cyano-3,4-bis(oxidanyl)oxolan-2-yl]methyl dihydrogen phosphate (F86).

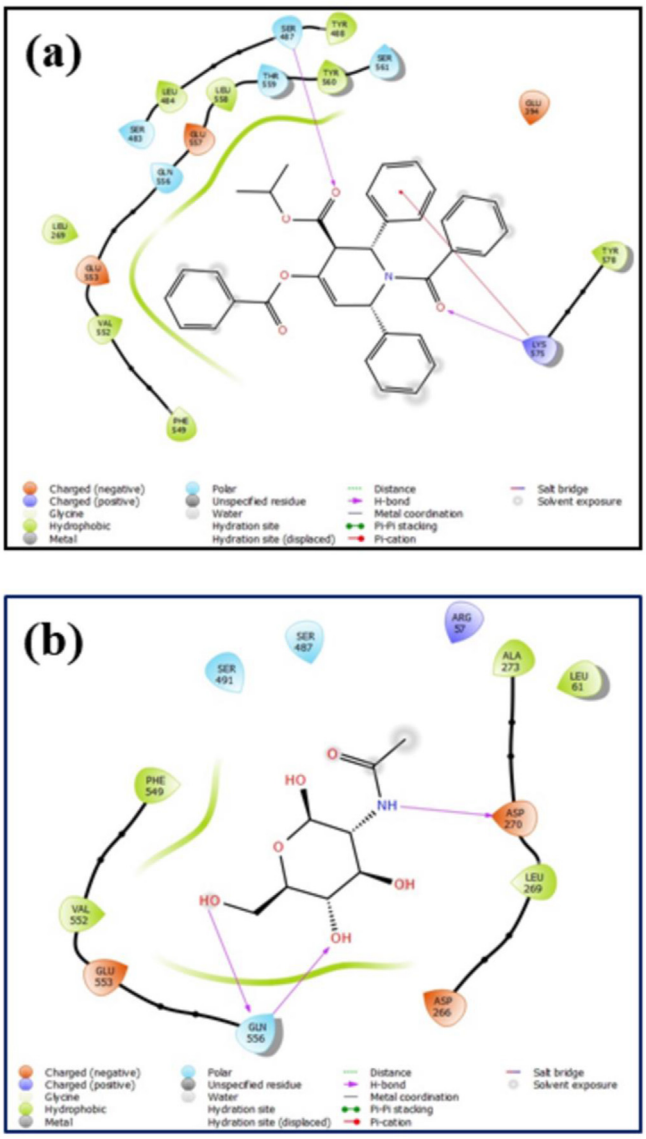


**Figure 15.** Docking interactions with 6M18 (a) IDPC (b) Co-ligand (2-acetamido-2-deoxy-beta-D-glucopyranose).

For ACE2 receptor (6M18), IDPC had a lower binding affinity of -3.658 kcal $mol^{-1}$ than the co-crystallized ligand, NAG (−4.933 kcal $mol^{-1}$). IDPC showed a pi-cationic interaction with LYS 575 via its phenyl ring, hydrogen bond interactions with LYS 575 and SER 489 via its carbonyl oxygen groups (Figure 15a) while its co-crystallized ligand (NAG) showed hydrogen bond interactions with GLN 556 via hydroxyl groups and ASP 270 via its amino hydrogen group (Figure 15b). Hydrogen bond interactions of ACE2 inhibitors with receptors have also been reported [106, 107]. The results revealed that IDPC shows tendency to inhibit COVID by binding to the active sites of the receptors, with the best anti-COVID activity observed with the Mpro. Similar to IDPC, the co-crystallized ligands interact with the receptors via heteroatoms and/or π-structure. This may be as a result of some carbonyl and/or aromatic functional similarities the co-crystallized ligands share with IDPC. The low values observed in the PLpro, RdRp and ACE2 receptors shows that IDPC could inhibit polyprotein maturation and consequently, abolish infectivity [108].

## 5. Conclusion

The synthesis and characterization (via x-ray crystallography, FT-IR and NMR) of IDPC is hereby reported. Geometrical parameters, normal vibrational modes, molecular properties ($E_{HOMO}$, $E_{LUMO}$, energy gap) and reactivity descriptors were calculated using density functional theory. X-ray crystallographic data agreed with optimized geometrical parameters. The assignment of calculated vibrational frequencies was achieved using scaled quantum mechanics force field. The selected experimental FT-IR wavenumbers for major vibrations (C–H, C=O, C=C and C–O) were consistent with the calculated vibrational modes. The frontier orbital energies and the low energy gap indicate intramolecular charge transfer tendency and good bioactivity of the compound. Topological (AIM, RDG, ELF, LOL, MESP) and Hirshfeld analyses confirm the presence of H-bonding, covalent and noncovalent interactions and electron delocalization in the molecule. Molecular docking of IDPC on four SARS-COVID proteins was achieved. Strong binding affinity observed between the active sites of the Mpro receptor and IDPC ligand was mainly attributed

to H-bonding and π-cationic interactions via the phenyl ring and the carbonyl oxygen groups resulting into good anti-COVID potentials of the compound by blocking polyprotein maturation.

## Declarations

### Author contribution statement

Arulraj Ramalingam: Conceived and designed the experiments; Performed the experiments; Contributed reagents, materials, analysis tools or data; Wrote the paper.

Murugavel Kuppusamy: Conceived and designed the experiments; Contributed reagents, materials, analysis tools or data; Wrote the paper.

Sivakumar Sambandam, Mouna Medimagh, Amirthaganesan Shanmugasundaram, Noureddine Issaoui: Analyzed and interpreted the data; Contributed reagents, materials, analysis tools or data.

Oluwatoba Emmanuel Oyeneyin: Performed the experiments; Analyzed and interpreted the data; Contributed reagents, materials, analysis tools or data, Wrote the paper.

Nathanael Damilare Ojo: Analyzed and interpreted the data; Wrote the paper.

### Funding statement

This research did not receive any specific grant from funding agencies in the public, commercial, or not-for-profit sectors.

### Data availability statement

Data included in article/supplementary material/referenced in article.

### Declaration of interests statement

The authors declare no conflict of interest.

### Additional information

Supplementary content related to this article has been published online at https://doi.org/10.1016/j.heliyon.2022.e10831.

## References

[1] E.B. Dennler, A.S. Frasca, Synthesis of fused heterocyclic compounds with polyphosphoric acid, Can. J. Chem. 45 (1967) 697–705.
[2] B. Abarca-gonzález, The chemistry of [1,2,3]Triazolo [1,5-a] pyridines, J. Enzym. Inhib. Med. Chem. 17 (2008) 359–367.
[3] B.T. Ogunyemi, O.E. Oyeneyin, O.T. Esan, I.A. Adejoro, Computational modelling and characterisation of phosphole adopted in triphenyl amine photosensitisers for solar cell applications, Res. Chem. 2 (2020), 100069.
[4] K. Lee, H. Nada, H.J. Byun, C.H. Lee, A. Elkamhawy, Hit identification of a novel quinazoline sulfonamide as a promising EphB3 inhibitor: design, virtual combinatorial library, synthesis, biological evaluation, and docking simulation studies, Pharmacy 14 (2021) 1–20.
[5] M. Maryška, L. Svobodov, W. Dehaen, M. Hrabinov, M. Rumlova, O. Soukup, M. Kuchar, Heterocyclic cathinones as inhibitors of kynurenine aminotransferase II—design, synthesis, and evaluation, Pharmacy 14 (2021) 1–20.
[6] K. Murugavel, S. Amirthaganesan, R.T. Sabapathy Mohan, A convenient synthesis and structural analysis of novel 4,5,6,7-tetrahydro-1H-indazoles, Chem. Heterocycl. Compd. 46 (2010) 302–306.
[7] Mennatallah Mahmoud Abdelshaheed, Iten Mamdouh Fawzy, Hussein Ibrahim El-Subbagh, Khairia Mohamed Youssef, Piperidine nucleus in the field of drug discovery, Fut. J. Pharm. Sci. 7 (2021) 188.
[8] G. Wang, L. Chen, T. Xian, Y. Liang, X. Zhang, Z. Yang, M. Luo, Discovery and SAR study of piperidine-based derivatives as novel infuenza virus inhibitors, Org. Biomol. Chem. 12 (2014) 8048–8060.
[9] Y. Pourshojaei, A. Abiri, K. Eskandari, Z. Haghighijoo, N. Edraki, A. Asadipour, Phenoxyethyl piperidine/morpholine derivatives as PAS and CAS inhibitors of cholinesterases: insights for future drug design, Sci. Rep. 9 (2019) 19855.
[10] S. Soumya, I.H. Joe, A combined experimental and quantum chemical study on molecular structure, spectroscopic properties and biological activity of anti-inflammatory Glucocorticosteroid drug, Dexamethasone, J. Mol. Struct. 1245 (2021) 1–15.
[11] R. Arulraj, S. Sivakumar, A. Thiruvalluvar, A. Manimekalai, Crystal Structure of "T-3-Benzyl-R- 2,c-6-Diphenylpiperidin-4-One Oxime, IUCrData, 2016, 161982.
[12] K. Rajkumar, S. Sivakumar, R. Arulraj, M. Kaur, J.P. Jasinski, A. Manimekalai, A. Thiruvalluvar, Crystal structures of two new 3-(2-chloroethyl)-r(2),c(6)-diarylpiperidin-4-ones, Acta Crystallogr. E E. E74 (2018) 483–486.
[13] R. Arulraj, S. Sivakumar, A. Thiruvalluvar, M. Kaur, J.P. Jasinski, 3-Chloro-r-2,c-6-bis(4-fluorophenyl)-3-methyl-piperidin-4-one, IUCrData 3 (2016).
[14] R. Arulraj, S. Sivakumar, M. Kaur, A. Thiruvalluvar, P. Jerry, Crystal structures of three 3-chloro-3-methyl-2,6-diarylpiperidin-4-ones, Crystal. Comm. E73 (2017) 107–111.
[15] R. Arulraj, S. Sivakumar, S. Suresh, K. Anitha, Synthesis, vibrational spectra, DFT calculations, Hirshfeld surface analysis and molecular docking study of 3-chloro-3-methyl-2,6-diphenylpiperidin-4-one, Spectrochim. Acta Part A: Molec. Biomolec. Spec. 232 (2020) 1–15, 118166.
[16] Y. Ling, Z.-Y. Hao, D. Liang, C.-L. Zhang, Y.-F. Liu, Y. Wang, The expanding role of pyridine and dihydropyridine scaffolds in drug design, Drug Des. Dev. Ther. 15 (2021) 4289–4338.
[17] M. Abdullahi, N. Das, S. Elijah, A. Kabiru, A. Muhammad, In-silico design and ADMET predictions of some new imidazo [1,2-a] pyridine-3-carboxamides (IPAs) as anti-tubercular agents, J. Clin. Tuber. Other Mycobac. Dis. 25 (2021), 100276.
[18] I.D. Agostino, I. Giacchello, G. Nannetti, A.L. Fallacara, F. Musumeci, G. Grossi, G. Palù, Y. Cau, M. Trist, A. Loregian, S. Schenone, M. Botta, Synthesis and biological evaluation of a library of hybrid derivatives as inhibitors of Influenza Virus PA-PB1 interaction, Eur. J. Med. Chem. 157 (2018) 743–758.
[19] A. Ghaleb, A. Aouidate, H. Ben, E. Ayouchia, H. Anane, S. Stiriba, A. Ghaleb, A. Aouidate, H. Ben, E. Ayouchia, A. Ghaleb, A. Aouidate, H. Ben, E. Ayouchia, M. Aarjane, H. Anane, In Silico molecular investigations of pyridine N- Oxide compounds as potential inhibitors of SARS- CoV-2: 3D QSAR, molecular docking modeling, and ADMET screening, J. Biomol. Struct. Dyn. 40 (1) (2022) 143–153.
[20] J. Balzarini, E. Keyaerts, L. Vijgen, F. Vandermeer, M. Stevens, E. De Clercq, H. Egberink, M. Van Ranst, Pyridine N-oxide derivatives are inhibitory to the human SARS and feline infectious peritonitis coronavirus in cell culture, J. Antimicrob. Chemother. 57 (2006) 472–481.
[21] https://covid19.who.int/, (n.d.).
[22] https://www.who.int/news-room/questions-and-answers/item/coronavirus-disease-(covid-19)- vaccines-safety, (n.d.) 19.
[23] https://www.fda.gov/news-events/press-announcements/fda-approves-first-treatment-covid-19, (n.d.).
[24] https://www.who.int/news-room/feature-stories/detail/who-recommends-against-the-use-of- remdesivir-in-covid-19-patients, (n.d.) 19.
[25] O.O. Oderinlo, O.A. Adenekan, T.T. Alawode, P.M. Osamudiamen, B.B. Oluremi, O.E. Oyeneyin, M.P. Ngoepe, Ethnobotanical appraisal and in-silico investigation of plants used for the management of COVID-19 in southwestern Nigeria, Arab. J. Medic. Arom. Plants. 7 (2021) 151–174.
[26] C. Mouffouk, S. Mouffouk, S. Mouffouk, L. Hambaba, H. Haba, Flavonols as potential antiviral drugs targeting SARS-CoV-2 proteases (3CLpro and PLpro), spike protein, RNA-dependent RNA polymerase (RdRp) and angiotensin-converting enzyme II receptor (ACE2), Eur. J. Pharmacol. 891 (2020), 173759.
[27] M.-F. Hsu, C.-J. Kuo, K.-T. Chang, H.-C. Chang, C.-C. Chou, T.-P. Ko, H.-L. Shr, G.-G. Chang, A.H.-J. Wang, P.-H. Liang, Mechanism of the maturation process of SARS-CoV 3CL protease mechanism of the maturation process of SARS-CoV 3CL protease, J. Biol. Chem. 280 (2005) 31257–31266.
[28] S. Bharadwaj, A. Dubey, U. Yadava, S.K. Mishra, Exploration of natural compounds with anti-SARS-CoV-2 activity via inhibition of SARS-CoV-2 Mpro, Briefings Bioinf. 22 (2021) 1361–1377.
[29] W. Rut, Z. Lv, M. Zmudzinski, S. Patchett, D. Nayak, S.J. Snipas, F. El Oualid, T.T. Huang, M. Bekes, M. Drag, S.K. Olsen, Activity profiling and crystal structures of inhibitor-bound SARS-CoV-2 papain-like protease: a framework for anti-COVID-19 drug design, Sci. Adv. 6 (2020) 4596.
[30] M. Hoffmann, H. Kleine-Weber, S. Schroeder, N. Krüger, T. Herrler, S. Erichsen, T.S. Schiergens, G. Herrler, N.-H. Wu, A. Nitsche, M.A. Müller, C. Drosten, S. Pöhlmann, SARS-CoV-2 cell entry depends on ACE2 and TMPRSS2 and is blocked by a clinically proven protease inhibitor, Cell 181 (2020) 271–280.
[31] Z. Wang, L. Yang, X. Zhao, Co-crystallization and structure determination: an effective direction for anti-SARS-CoV-2 drug discovery, Comput. Struct. Biotechnol. J. 19 (2021) 4684–4701.
[32] C. Lin, F.-J. Tsai, Y.-M. Hsu, T.-J. Ho, G.-K. Wang, Y.-J. Chiu, J.-S. Yang, Study of Baicalin toward COVID-19 treatment: in silico target analysis and in vitro inhibitory effects on SARS-CoV-2 proteases, Biomed. Hub. 6 (2021) 122–137.
[33] H. Liu, F. Ye, Q. Sun, H. Liang, C. Li, S. Li, R. Lu, B. Huang, W. Tan, L. Lai, Scutellaria baicalensis extract and baicalein inhibit replication of SARS-CoV-2 and its 3C-like protease in vitro, J. Enzym. Inhib. Med. Chem. 36 (2021) 497–503.
[34] A. Frediansyah, F. Nainuc, K. Dhama, M. Mudatsir, H. Harapan, Remdesivir and its antiviral activity against COVID-19: a systematic review, Clin. Epidemiol. Glob. Health. 9 (2021) 123–127.
[35] F.I. Khan, T. Kang, H. Ali, D. Lai, Remdesivir strongly binds to RNA-dependent RNA polymerase, membrane protein, and main protease of SARS-CoV-2: indication from molecular modeling and simulations, Front. Pharmacol. 12 (2021) 1–14.
[36] W. Wang, X. Zhao, W. Wei, W. Fan, K. Gao, S. He, X. Zhuang, Angiotensin-converting enzyme inhibitors (ACEI) or angiotensin receptor blockers (ARBs) may be safe for COVID-19 patients, BMC Infect. Dis. 21 (2021) 1–8.
[37] F. Rugg-gunn, Adverse effects and safety profile of perampanel: a review of pooled data, Epilepsia 55 (2014) 13–15.
[38] K. Sriram, P.A. Insel, Risks of ACE inhibitor and ARB usage in COVID-19: evaluating the evidence, Clin. Pharmacol. Therapeut. 108 (2020) 236–241.

[39] https://www.drugs.com/mtm/remdesivir.html, (n.d.).
[40] https://www.fda.gov/drugs/human-drug-compounding/fda-alerts-health-care-professionals-and- compounders-potential-risks-associated-compounding, (n.d.).
[41] F.E. Ani, C.U. Ibeji, N.L. Obasi, M.T. Kelani, K. Ukogu, G.F. Tolufashe, S.A. Ogundare, O.E. Oyeneyin, G.E.M. Maguire, H.G. Kruger, Crystal, spectroscopic and quantum mechanics studies of Schiff bases derived from 4-nitrocinnamaldehyde, Sci. Rep. 11 (2021) 1–11.
[42] A. Ramalingam, S. Kansız, N. Dege, S. Sambandam, Synthesis, crystal structure, DFT calculations and hirshfeld surface analysis of 3-chloro-2,6-bis(4-chlorophenyl)-3-methylpiperidin-4-one, J. Chem. Crystallogr. 51 (2020) 273–287.
[43] O.A. Odewole, C.U. Ibeji, H.O. Oluwasola, O.E. Oyeneyin, K.G. Akpomie, C.M. Ugwu, C.G. Ugwu, T.E. Bakare, Synthesis and anti-corrosive potential of Schiff bases derived 4-nitrocinnamaldehyde for mild steel in HCl medium: experimental and DFT studies, J. Mol. Struct. 1223 (2021) 1–9.
[44] O. Noureddine, S. Gatfaoui, S.A. Brandán, H. Marouani, N. Issaou, Structural, docking and spectroscopic studies of a new piperazine derivative, 1-phenylpiperazine-1,4-diium-bis (hydrogen sulfate), J. Mol. Struct. 1202 (2019), 127351.
[45] A. Kumar, S. Sambandam, A. Ramalingam, K. Rajkumar, M. Kaur, J.P. Jasinski, Synthesis, crystal structure, DFT calculations and Hirshfeld surface analysis of 3-butyl-2,6-bis(4-fluorophenyl)piperidin-4-one, Acta Crystallogr. E. E76 (5) (2020) 651–655.
[46] N.D. Ojo, R.W. Krause, N.O. Obi-Egbedi, Electronic and nonlinear optical properties of 2-(((5-aminonaphthalen-1-yl)imino)methyl)phenol: experimental and time-dependent density functional studies, Journal of Molecular Liquids 319 (2020) 1–8, 114157.
[47] O.F. Akinyele, A.S. Adekunle, D.S. Olayanju, O.E. Oyeneyin, S.S. Durodola, N.D. Ojo, A.A. Akinmuyisitan, T.A. Ajayeoba, L.O. Olasunkanmi, Synthesis and corrosion inhibition studies of (E)-3-(2-(4–chloro-2-nitrophenyl)diazenyl)-1-nitrosonaphthalen-2-ol on mild steel dissolution in 0.5 M HCl solution-experimental, DFT and Monte Carlo simulations, J. Mol. Struct. 1268 (2022), 133738.
[48] A. Ramalingam, S. Sambandam, M. Medimagh, O. Al-Dossary, N. Issaoui, M.J. Wojcik, Study of a new piperidone as an anti-Alzheimer agent: molecular docking, electronic and intermolecular interaction investigations by DFT method, J. King Saud Univ. Sci. 33 (8) (2021), 101632.
[49] A. Ramalingam, Hirshfeld surface analysis, interaction energy calculation and spectroscopical study of 3-chloro-3-methyl-r(2),c(6)-bis(p-tolyl)piperidin-4-one using DFT approaches, J. Mol. Struct. 1248 (2022), 131483.
[50] O. Oyeneyin, D. Akerele, N. Ojo, O. Oderinlo, Corrosion inhibitive potentials of some 2H-1-benzopyran-2-one derivatives- DFT calculations, Biointerf. Res. Appl. Chem. 11 (2021) 13968–13981.
[51] A.A. Olanrewaju, C.U. Ibeji, O.E. Oyeneyin, Biological evaluation and molecular docking of some newly synthesized 3d-series metal(II) mixed-ligand complexes of fluoro-naphthyl diketone and dithiocarbamate, SN Appl. Sci. 2 (2020) 678.
[52] O.E. Oyeneyin, B.S. Obadawo, D.S. Metibemu, T.O. Owolabi, A.A. Olanrewaju, S.M. Orimoloye, N. Ipinloju, O. Olubosede, An exploration of the antiproliferative potential of chalcones and dihydropyrazole derivatives in prostate cancer via androgen receptor: combined QSAR, machine learning, and molecular docking techniques, Phys. Chem. Res. 10 (2022) 211–223.
[53] A. Ramalingam, N. Mustafa, W.J. Chng, M. Medimagh, S. Sambandam, N. Issaoui, 3-Chloro-3-methyl-2,6-diarylpiperidin-4-ones as anti-cancer agents: synthesis, biological evaluation, molecular docking, and in silico ADMET prediction, Biomolecules 12 (8) (2022) 1–22, 1093.
[54] O.E. Oyeneyin, B.S. Obadawo, S.M. Orimoloye, E.O. Akintemi, N. Ipinloju, A.M. Asere, T.O. Owolabi, Prediction of inhibition activity of BET bromodomain inhibitors using grid search-based extreme learning machine and molecular docking, Lett. Drug Des. Discov. 18 (2021) 1039–1049.
[55] O.E. Oyeneyin, Tuning the electronic and nonlinear optical properties of (4-methylphenyl) (4-methylpiperidin-1-yl) methanone and its substituted analogues, Sci. Lett. 9 (2021) 49–54.
[56] F. Bardak, C. Bardak, C. Karaca, E. Kose, S. Bilgili, A. Atac, Anionic dependency of electronic and nonlinear optical properties of ionic liquids, J. Mol. Liq. 345 (2022), 117030.
[57] D. Cappello, F.L. Buguis, J.B. Gilroy, Tuning the properties of donor–acceptor and acceptor–donor–acceptor boron difluoride hydrazones *via* extended π-conjugation, ACS Omega 7 (2022) 32727–32739.
[58] A. Kumar, S. Sambandam, A. Ramalingam, R. Krishnamoorthy, D. Arumugam, O.E. Oyeneyin, Synthesis, molecular docking of 3-(2-chloroethyl)-2,6-diphenylpiperidin-4-one: hirshfeld surface, spectroscopic and DFT based analyses, J. Mol. Struct. 1262 (2022), 132993.
[59] R. Sukanya, D. Aruldhas, I. Hubert Joe, S. Balachandran, Spectroscopic and quantum chemical computation on molecular structure, AIM, ELF, RDG, NCI, and NLO activity of 4-VINYL benzoic acid: a DFT approach, J. Mol. Struct. 1253 (2022), 132273.
[60] C.D. Vincy, J.D.D. Tarika, X.D.D. Dexlin, A. Rathika, T.J. Beaula, Exploring the antibacterial activity of 1,2-diaminoethane hexanedionic acid by spectroscopic, electronic, ELF, LOL, RDG analysis and molecular docking studies using DFT method, J. Mol. Struct. 1247 (2022), 131388.
[61] X.D.D. Dexlin, J.D.D. Tarika, S.R. Kumar, A. Mariappan, T.J. Beaula, Synthesis and DFT computations on structural, electronic and vibrational spectra, RDG analysis and molecular docking of novel Anti COVID-19 molecule 3, 5 Dimethyl Pyrazolium 3, 5 Dichloro Salicylate, J. Mol. Struct. 1246 (2021) 1–17, 131165.
[62] S.P. Yeddu, P. Thangaiyan, A. Veeraiah, D. Vijay, K.E. Srikanth, A. Irfan, R. Thomas, Vibrational spectral studies, quantum mechanical properties, and biological activity prediction and inclusion molecular self-assembly formation of n-n'-dimethylethylene urea, Biointerf. Res. Appl. Chem. 12 (2022) 3996–4017.
[63] H.N. Malik, A. Jabeen, S. Ashraf, Z.U. Haq, U. Salar, Arshia, K.M. Khan, Benzophenone and coumarin derivatives as 3-CLPro inhibitors: targeting cytokine storm through in silico and in vitro approaches, J. Mol. Struct. 1265 (2022), 133478.
[64] E.R. Esharkawy, F. Almalki, T. Ben Hadda, In vitro potential antiviral SARS-CoV-19- activity of natural product thymohydroquinone and dithymoquinone from Nigella sativa, Bioorg. Chem. 120 (2022) 1–9.
[65] M.S.M. Abd El Hafez, M.G. AbdEl-Wahab, M.G. Seadawy, M.F. El-Hosseny, O. Beskales, A. Saber Ali Abdel-Hamid, M.A. El Demellawy, D.A. Ghareeb, Characterization, in-silico, and in-vitro study of a new steroid derivative from Ophiocoma dentata as a potential treatment for COVID-19, Sci. Rep. 12 (2022) 1–11.
[66] M.T. Quimque, K.I. Notarte, A. Letada, R.A. Fernandez, D.Y. Pilapil, K.R. Pueblos, J.C. Agbay, H.M. Dahse, A. Wenzel-Storjohann, D. Tasdemir, A. Khan, D.Q. Wei, A.P. Gose Macabeo, Potential cancer- and alzheimer's disease-targeting phosphodiesterase inhibitors from uvaria alba: insights from in vitro and consensus virtual screening, ACS Omega 6 (2021) 8403–8417.
[67] M.A. Abu-Zaied, G.H. Elgemeie, F.T. Halaweish, S.F. Hammad, Synthesis of novel pyridine and pyrimidine thioglycoside phosphoramidates for the treatment of COVID-19 and influenza A viruses, Nucleos Nucleot. Nucleic Acids 41 (2022) 851–877.
[68] K.C. Badgujar, A.H. Ram, R. Zanznay, H. Kadam, V.C. Badgujar, Remdesivir for COVID-19: a review of pharmacology, mechanism of action, in-vitro activity and clinical use based on available case studies, J. Drug Deliv. Therapeut. 10 (2020) 264–270.
[69] E. Govindan, K. Murugavel, S. Amirthaganesan, A. Subbiahpandi, Isopropyl 1-benzoyl-4-benzoyloxy-2,6-diphenyl-1,2,3,6-tetrahydropyridine-3-carboxylate, Acta Crystallogr. E E. E70 (2014), 0854.
[70] K.A. Begam, N. Kanagathara, M.K. Marchewka, A. Lo, DFT, hirshfeld and molecular docking studies of a hybrid compound -2,4-Diamino-6-methyl-1,3,5-triazin-1-ium hydrogen oxalate as a promising anti -breast cancer agent, Heliyon 8 (2022), e10355.
[71] M.J. Frisch, G.W. Trucks, H.B. Schlegel, G.E. Scuseria, M.A. Robb, J.R. Cheeseman, G. Scalmani, V. Barone, B. Mennucci, G.A. Petersson, H. Nakatsuji, M. Caricato, X. Li, H.P. Hratchian, A.F. Izmaylov, J. Bloino, G. Zheng, J.L. Sonnenberg, M. Hada, M. Ehara, K. Toyota, R. Fukuda, J. Hasegawa, M. Ishida, T. Nakajima, Y. Honda, O. Kitao, H. Nakai, T. Vreven, J. Montgomery, J.E. Peralta, F. Ogliaro, M. Bearpark, J.J. Heyd, E. Brothers, K.N. Kudin, V.N. Staroverov, R. Kobayashi, J. Normand, K. Raghavachari, A. Rendell, J.C. Burant, S.S. Iyengar, J. Tomasi, M. Cossi, N. Rega, N.J. Millam, M. Klene, J.E. Knox, J.B. Cross, V. Bakken, C. Adamo, J. Jaramillo, R. Gomperts, R.E. Stratmann, O. Yazyev, A.J. Austin, R. Cammi, C. Pomelli, J.W. Ochterski, R.L. Martin, K. Morokuma, V.G. Zakrzewski, G.A. Voth, P. Salvador, J.J. Dannenberg, S. Dapprich, A.D. Daniels, Ö. Farkas, J.B. Foresman, J.V. Ortiz, J. Cioslowski, D. Fox, Gaussian 09, Revision C.01, Gaussian, Inc., 2009.
[72] G.A. Zhurko, D.A. Zhurko, Chemcraft-graphical Program for Visualization of Quantum Chemistry Computations, Trial version, 2005.
[73] T. Lu, F. Chen, Multiwfn: a multifunctional Wavefunction analyzer, J. Comput. Chem. 33 (2012) 580e592.
[74] W. Humphrey, A. Dalke, K. Schulten, VMD: visual molecular dynamics, J. Mol. Graph. 14 (1996) 33–38.
[75] N.O. Obi-Egbedi, N.D. Ojo, Synthesis, light harvesting efficiency, photophysical and nonlinear optical properties of 3-(5-(4-hydroxybenzylideneamino) naphthalen-1-yliminomethyl)phenol: spectroscopic and quantum chemical approach, Res. Chem. Intermed. 47 (2021) 5249–5266.
[76] GaussView, Guassian, Inc., Carnergie Office Parck-Building6 Pittsburgh PA 151064 USA), Copyright © 2000-2003, Semichem. Inc., 2003, 151064.
[77] https://www.rcsb.org/, (n.d.).
[78] G. Madhavi Sastry, M. Adzhigirey, T. Day, R. Annabhimoju, W. Sherman, Protein and ligand preparation: parameters, protocols, and influence on virtual screening enrichments, J. Comp.-Aid. Molec. Des. 27 (2013) 221–234.
[79] Schrödinger Release 2021-3, LigPrep, Schrödinger, LLC, New York, NY, 2021 (n.d.).
[80] T. Halgren, Identifying and characterizing binding sites and assessing druggability, J. Chem. Inf. Model. 49 (2009) 377–389.
[81] P.C.S., D.T.M.R.A. Friesner, R.B. Murphy, M.P. Repasky, L.L. Frye, J.R. Greenwood, T.A. Halgren, Extra precision glide: docking and scoring incorporating a model of hydrophobic enclosure for protein-ligand complexes, J. Med. Chem. 49 (2006) 6177–6196.
[82] K. Pandiyarajan, R.T. Sabapathy Mohan, K. Murugavel, R. Hema, Synthesis and conformational study of some r(2),c(4)-bis(isopropoxycarbonyl)-t(3)-aryl-c(5)-hydroxy-t(5)-methylcyclohexanones using NMR spectra, J. Mol. Struct. 875 (2008) 226–234.
[83] G. Aridoss, S. Balasubramanian 1, P. Parthiban, S. Kabilan, Spectrochim. Acta, Part A 68 (2007) 1153–1163.
[84] M. Krishna Pillai, R. Krishna kumar, Arumugam Nagarajan, G. Jeyaraman- Indi, J. Chem. Soc. B 39B (2000) 419–425.
[85] A. Dhandapani, S. Veeramanikandan, R.S. Kumar, A.I. Almansour, N. Arumugam, S. Subashchandrabose, J. Suresh, R. Arulraj, D. Gajalakshmi, Synthesis, in vitro and in silico antitumor evaluation of 3-(2,6-dichlorophenyl)-1,5-diphenylpentane-1,5-dione: structure, spectroscopic, RDG, Hirshfeld and DFT based analyses, J. Mol. Struct. 1251 (2021), 132002.
[86] R.F.W. Bader, M.A. Austen, Properties of atoms in molecules: atoms under pressure, J. Chem. Phys. 107 (1997) 4271–4285.

[87] M. Medimagh, N. Issaoui, S. Gatfaoui, S.A. Brandán, O. Al-Dossary, H. Marouani, M.J. Wojcik, Impact of non-covalent interactions on FT-IR spectrum and properties of 4- methylbenzylammonium nitrate. A DFT and molecular docking study, Heliyon 7 (2021), e08204, 1–26.
[88] A. Kazachenko, F. Akman, M. Medimagh, N. Issaoui, N. Vasilieva, Y.N. Malyar, O.M. Al Dossary, Sulfation of diethylaminoethyl-cellulose: QTAIM topological analysis and experimental and DFT studies of the properties, ACS Omega 6 (2021) 22615.
[89] R.A. Boto, J. Contreras-garcía, J. Tierny, J. Piquemal, R.A. Boto, J. Contreras-garcía, J. Tierny, Interpretation of the reduced density gradient, Mol. Phys. 114 (2015) 1406–1414.
[90] J.D.D. Tarika, X.D.D. Dexlin, S. Madhankumar, D.D. Jayanthi, T.J. Beaula, Tuning the computational evaluation of spectroscopic, ELF, LOL, NCI analysis and molecular docking of novel anti COVID-19 molecule 4-dimethylamino pyridinium 3, 5-dichlorosalicylate, Spectrochim. Acta, Part A 259 (2021) 1–17.
[91] F.R. B., J.C. Prasana, S. Muthu, C.S. Abraham, Molecular docking studies, charge transfer excitation and wave function analyses (ESP, ELF, LOL) on valacyclovir : a potential antiviral drug, Comput. Biol. Chem. 78 (2019) 9–17.
[92] A. Shafi, R.D. Timiri Sathyamurthy, J. Seetharaman, M. Sambanthan, R. Murugesan, S. Sundaram, R. Bhanumathy Ramarathinam, Molecular docking, quantum chemical computational and vibrational studies on bicyclic heterocycle "6-nitro-2,3-dihydro-1,4-benzodioxine": anti-cancer agent, Comput. Biol. Chem. 86 (2020) 1–15.
[93] O.E. Oyeneyin, DFT and monte carlo simulations on the corrosion inhibitive potentials of some furan-based carbohydrazide derivatives, Lett. Appl. NanoBioSci. 12 (4) (2023) 1–22, 113.
[94] O.E. Oyeneyin, N.D. Ojo, N. Ipinloju, A.C. James, E.B. Agbaffa, Investigation of corrosion inhibition potentials of some aminopyridine schiff bases using density functional theory and Monte Carlo simulation, Chem. Afr. 5 (2022) 319–322.
[95] O.E. Oyeneyin, N. Ipinloju, D.D. Akerele, Structural modification of ibuprofen as new NSAIDs via DFT , molecular docking and pharmacokinetics studies, Int. J. Adv. Engin. Pure Sci. 33 (2021) 614–626.
[96] N.D. Ojo, R.W. Krause, N.O. Obi-Egbedi, Electronic and nonlinear optical properties of 3-(((2-substituted-4-nitrophenyl)imino)methyl)phenol, Computat. Theor. Chem. 1192 (2020) 1–8.
[97] S. Selvakumari, C. Venkataraju, S. Muthu, A. Irfan, A. Saral, Evaluation of electronic properties in different solvents, spectroscopic exposition (FT-IR, FT-Raman), and molecular docking studies of 5-Chloro-2-hydroxypyridine - insulysin inhibitor, J. Mol. Liq. 341 (2021) 1–11.
[98] M. Ashfaq, K.S. Munawar, G. Bogdanov, A. Ali, M.N. Tahir, G. Ahmed, A. Ramalingam, M.M. Alam, M. Imran, S. Sambandam, B. Munir, Single crystal inspection, Hirshfeld surface investigation and DFT study of a novel derivative of 4-fluoroaniline: 4-((4-fluorophenyl)amino)-4-oxobutanoic acid (BFAOB), J. Iran. Chem. Soc. 19 (2022) 1953–1961.
[99] S. Jiang, Y. Jin, R. Yan, Z. Wang, Detailed structural study of cyclic anticancer drug Lorlatinib: spectroscopic and stereostructure investigation (IR, ECD and NMR) using density functional theory approach, J. Mol. Struct. 1225 (2021) 1–11.
[100] G. Khalsa, N.A. Benedek, J. Moses, Ultrafast control of material optical properties via the infrared resonant Raman effect, Phys. Rev. X. 11 (2021) 1–16.
[101] T.N. Moroz, H.G.M. Edwards, The use of Raman and infrared spectroscopy in determining the space symmetry group among the groups with the same rules of systematic absence in the diffraction patterns: some basic principles and applications, J. Raman Spectrosc. 52 (2021) 2058–2067.
[102] R. Arulraj, Synthesis, crystal structure, DFT calculations and hirshfeld surface analysis of 3-Chloro-3-methyl-r(2),c(6)-bis(p-methoxyphenyl)piperidin-4-one, J. Chem. Crystallogr. 50 (2020) 41–51.
[103] R. Arulraj, R.G. Ahlam, S. Sivakumar, K. Anitha, K. Rajkumar, B. Nourdine, C. Abdelkader, M. Elayaperumal, Synthesis, vibrational spectra, Hirshfeld surface analysis, DFT calculations, and in silico ADMET study of 3-(2-chloroethyl)-2,6-bis(4-fluorophenyl)piperidin-4-one: a potent anti-Alzheimer agent, J. Mol. Struct. 1269 (2022), 133845.
[104] N.D. Gajjar, T.M. Dhameliya, G.B. Shah, In search of RdRp and Mpro inhibitors against SARS CoV-2: molecular docking, molecular dynamic simulations and ADMET analysis, J. Mol. Struct. 1239 (2021), 130488.
[105] S. Singh, M.F. Sk, A. Sonawane, P. Kar, S. Sadhukhan, Plant-derived natural polyphenols as potential antiviral drugs against SARS-CoV-2 via RNAdependent RNA polymerase (RdRp) inhibition: an in-silico analysis, J. Biomol. Struct. Dyn. 39 (2021) 6249–6264.
[106] A. Basu, A. Sarkar, U. Maulik, Molecular docking study of potential phytochemicals and their effects on the complex of SARS-CoV2 spike protein and human ACE2, Sci. Rep. 10 (2020), 17699.
[107] A.A. Al-Karmalawy, M.A. Dahab, A.M. Metwaly, S.S. Elhady, E.B. Elkaeed, I.H. Eissa, K.M. Darwish, Molecular docking and dynamics simulation revealed the potential inhibitory activity of ACEIs against SARS-CoV-2 targeting the hACE2 receptor, Front. Chem. 9 (2021), 661230.
[108] F.K.M. Schur, M. Obr, W.J.H. Hagen, W. Wan, A.J. Jakobi, J.M. Kirkpatrick, C. Sachse, H.-G. Krausslich, J.A. Briggs, An atomic model of HIV-1 caspid-SP1 reveals structures regulating assembly and maturation, Science 353 (2016), 5060508.